



# Automated quantitative diagnosis of GaAs solar cells using the CBAM-MS-1DCNN model on absolute electroluminescence imaging and distributed circuit modeling

WENJIE ZHOU,<sup>1,†</sup> PANPAN YANG,<sup>1,†</sup> YOUYANG WANG,<sup>2,†</sup> MANG ZHA,<sup>1</sup> DEYANG QIN,<sup>1</sup> QIAO HUANG,<sup>1</sup> GUOEN WENG,<sup>1</sup> XIAOBO Hu,<sup>1</sup> HIDEFUMI AKIYAMA,<sup>3</sup> JUNHAO CHU,<sup>4</sup> AND SHAOQIANG CHEN<sup>1,3,5,6,\*</sup>

<sup>1</sup>State Key Laboratory of Precision Spectroscopy, Department of Electronic Engineering, East China Normal University, 500 Dongchuan Road, Shanghai 200241, China

<sup>2</sup>School of Microelectronics (School of Integrated Circuits), Nanjing University of Science and Technology, Nanjing 210094, China

<sup>3</sup>Institute for Solid State Physics, The University of Tokyo, Kashiwanoha 5-1-5, Kashiwa, Chiba 2778581, Japan

<sup>4</sup>Institute of Optoelectronics, Fudan University, Shanghai 200433, China

<sup>5</sup>Joint Research Center of Light Manipulation Science and Photonic Integrated Chip of East China Normal University and Shandong Normal University, East China Normal University, Shanghai 200241, China

<sup>6</sup>Shanghai Key Laboratory of Multidimensional Information Processing, East China Normal University, Shanghai 200241, China

<sup>†</sup>These authors contributed equally to this work.

\*sqchen@ee.ecnu.edu.cn

Received 15 January 2025; revised 25 March 2025; accepted 5 April 2025; posted 7 April 2025; published 23 April 2025

Three-dimensional distributed circuit modeling based on SPICE software can simulate the electrical performance and the uniformity of electroluminescence (EL) intensity. To solve the problem that traditional methods require manual iteration to determine the device parameters of the simulation model, we proposed an efficient automated quantitative analysis method that can quickly diagnose the localized series resistor ( $R_{S-MC}$ ) of the dark-spot defects in GaAs solar cells via absolute EL images. This method employs a one-dimensional convolutional neural network model based on a multi-scale and convolutional block attention module (CBAM-MS-1DCNN). A medium dataset consisting of 200,000 defects from 250 simulated solar cells to train the CBAM-MS-1DCNN model, where the coefficient of determination ( $R^2$ ) > 0.95 and the normalized root mean square error (NRMSE) < 5%, indicating that the proposed model can predict  $R_{S-MC}$  well. Furthermore, the relative error of the predicted absolute EL intensity based on real samples can be controlled within 10% using the CBAM-MS-1DCNN model. The model trained on the simulated dataset has good prediction performance for real GaAs solar cells, which provides ideas for the problem of obtaining EL image datasets. © 2025 Optica Publishing Group. All rights, including for text and data mining (TDM), Artificial Intelligence (AI) training, and similar technologies, are reserved.

<https://doi.org/10.1364/AO.555991>

## 1. INTRODUCTION

Over the past several decades, several countries have begun to address their energy shortages. Solar energy, as an important type of renewable and clean energy, has been receiving increasing attention. Furthermore, the conversion efficiency of solar cells has been improving year-on-year [1]. However, solar cells often exhibit defects due to both internal and external influences, such as chemical or structural alterations resulting from prolonged exposure to various conditions like soaking, mechanical and thermal stresses, and high humidity levels [2–4]. These defects can adversely affect the spatial consistency of the cell and lead to a significant reduction in its conversion efficiency.

Consequently, developing an effective defect analysis approach is essential for providing critical insights into the design and fabrication of solar cells.

Characterization techniques of solar cells can be categorized into electrical testing techniques (ETTs) and imaging-based techniques (IBTs) [5]. In practice, ETTs such as current–voltage ( $I-V$ ) curve analysis [6–8], time domain reflectometry (TDR) [9], and capacitance–voltage ( $C-V$ ) measurements can characterize the condition of the entire cell [10–12], but are considered invasive and have difficulty in identifying local defects. IBTs, including infrared, thermal imaging [13–15], and electroluminescence methods [16–20], are considered non-intrusive and can effectively characterize local defects. EL imaging technology

**Table 1.** Summary of AI Methods for Solar Cell Defect Detection and Classification

Reference	Publication Year	AI Techniques Used	Dataset	Evaluation Metrics
Luo <i>et al.</i> [33]	2019	GAN, CNN	Synthetic	Accuracy improvement: 14% (GAN-augmented dataset)
Ahmad <i>et al.</i> [34]	2020	SVM, CNN	Public	Accuracy: 91.58% (CNN), 68.90%–72.74% (SVM)
Chen <i>et al.</i> [35]	2022	Random Forest, ResNet, YOLO	Real-world	Macro F1: 0.83 (ResNet18), 0.78 (YOLO)
Kellil <i>et al.</i> [36]	2023	CNN, VGG-16	Real-world	Accuracy: 99.91% (fault detection), 99.80% (fault diagnosis)
Acikgoz <i>et al.</i> [37]	2023	CNN, Inception-v3	Public	Accuracy: 93.59%
Liu <i>et al.</i> [38]	2024	EfficientNet-B0	Public	Accuracy: 97.81%, Precision: 97.70%, Recall: 97.59%, F1-score: 97.64%, MCC: 97.32%
Demirci <i>et al.</i> [39]	2024	GAN, CNN, VGG-16	Hybrid	Mean accuracy: 94.11% (public dataset), 93.08% (custom real-world dataset)

is commonly used to visualize defects in solar cells due to its suitability for small-scale deployment, not being easily affected by external factors, high efficiency in distinguishing internal and external defects, and support for quantitative analysis of local electrical characteristics.

The distributed equivalent circuit model, commonly employed for quantitative analysis in EL imaging, is often based on integrated circuit emphasis (SPICE). This model represents the solar cell as a network of microcells, each typically modeled using a single-diode or two-diode configuration [21–23]. These microcells correspond to the pixel regions of the EL image in position, and defects are artificially constructed through numerical simulations. The simulated solar cell has almost identical electrical performance and uniformity when compared with the actual one, so it can be considered a “digital twin” of the actual cell. Roy and Gupta [24] applied a distributed diode model to accurately quantify the shunt resistance of c-Si solar cells. Their simulation approach provided valuable insights into the electrical behavior of these cells under varying conditions. In contrast, Kikelj *et al.* [25] introduced a novel modeling technique that incorporates the PVMOS 2.5D workflow, leveraging the SPICE simulation platform. This approach was specifically designed to investigate the influence of various defects and imperfections, including both inactive and active cracks, disconnections in the finger grid, and regions of the cell that are non-functional (dead cell areas), on the resulting EL profile. By analyzing these individual factors, the study revealed how each defect type contributes to the degradation of the EL signal, offering crucial insights for improving solar cell design and performance. Chen *et al.* proposed absolute EL technology [26] and combined it with three-dimensional (3D) distributed circuit modeling to diagnose defects in solar cells [27–29]. The reliability and practicality of this method have been proven and used to diagnose defects caused by various factors, such as lasers and stress [30–32]. However, quantitative analysis methods

based on the distributed equivalent circuit model often require manual iteration to determine the simulation parameters of defects, which is time-consuming for solar cells with a large number of defects. To enhance the efficiency of defect diagnosis, it is essential to construct a method that can precisely predict parameters in an automated and streamlined manner. Such an approach would significantly reduce manual intervention, offering a faster and more reliable way to assess and address defects in the system.

Recent advancements in machine learning, particularly CNNs, have led to their widespread adoption for the automated detection and classification of EL defects. As shown in Table 1, we provide a summary of various AI-driven defect detection and classification techniques. The table summarizes different AI techniques, evaluation metrics, and datasets used from recent studies, offering a clear overview of the current advancements in the field.

We present a novel approach for automated quantitative analysis that integrates absolute EL images with the distributed equivalent circuit model. The absolute EL images of an industrial-grade GaAs solar cell are captured using a CCD camera. These images are then calibrated to account for relative light intensity, ensuring accurate measurements and analysis of the cell’s performance. Based on our previous research findings that the defects characterized by dark spots on absolute EL images of GaAs solar cells are linked to an increase in  $R_{S-MC}$  [28], we designed and trained a CNN regression model called CBAM-MS-1DCNN to accelerate the calculation of  $R_{S-MC}$  based on a simulated dataset. The proposed model has good predictive performance for both simulated solar cells and real samples, showcasing the practicality and universality of this method. The proposed method can help researchers rapidly establish a high-precision distributed equivalent circuit model of solar cells, which is an excellent quantitative approach for diagnosing solar-cell defects.

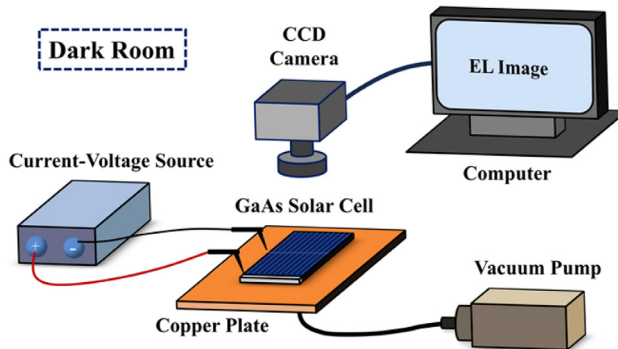


**Fig. 1.** Overview of the experimental setup for measuring absolute electroluminescence.

## 2. EXPERIMENT AND SIMULATION

### A. Experimental Setup

In our study, we employed an industrial-grade single-junction GaAs solar cell with dimensions of  $4\text{ cm} \times 2\text{ cm}$  as the sample. The experiments were carried out in a controlled dark box at  $25^\circ\text{C}$ . The GaAs solar cell was mounted on a custom copper (Cu) plate. A Si CCD camera (Hamamatsu C8484-05C), with a resolution of  $1920 \times 1080$  pixels, was positioned above the copper plate, as illustrated in Fig. 1. We injected a forward current through a current–voltage source (Keithley 2400) to capture EL images of the sample and measured its  $J - V$  characteristics.

The netlist files for the distributed equivalent circuit models in this study were all generated using our team's proprietary software, "Netlist Generator," as shown in Fig. 2. The software

provides an interactive and visualized circuit design environment, allowing users to quickly configure defect locations, quantities, and electrical parameters. It automatically generates netlist files for distributed circuit models compatible with SPICE, ensuring high efficiency in model construction. This software is a proprietary technology developed by our team, and the specific technical details of its design and implementation are not included in this paper.

### B. Modeling of an Equivalent Circuit Model

The SPICE software was used to establish the distributed equivalent circuit model of the sample, and defect analysis was performed on the simulation model. Figure 3(a) illustrates the structure of the GaAs solar cell sample, where a 3D distributed equivalent circuit model is employed to equivalently represent each layer of material as the corresponding electronic component, following the growth sequence of the solar cell materials. Next, the device can be further miniaturized into a structure of multiple microcells connected in series and parallel. In this work, the individual microcells of the sample cell are modeled using a two-diode approach. Specifically, under LED operation, each microcell is represented by several key components, including  $R_{\text{TOP}}$ ,  $R_{S-\text{MC}}$ ,  $R_{\text{SH-MC}}$ ,  $R_{\text{BOT}}$ , and  $D_1/D_2$ , with their characteristics being defined by  $J_{\text{MC}}$  and  $n_{\text{MC}}$ . This configuration is depicted in Fig. 3(b). Figure 3(c) illustrates the 3D equivalent circuit model, providing a detailed schematic diagram of the system.

We initially extracted the basic parameters ( $J$ ,  $n$ ,  $R_S$ , and  $R_{\text{SH}}$ ) of the entire model by fitting the  $J - V$  curve measured in

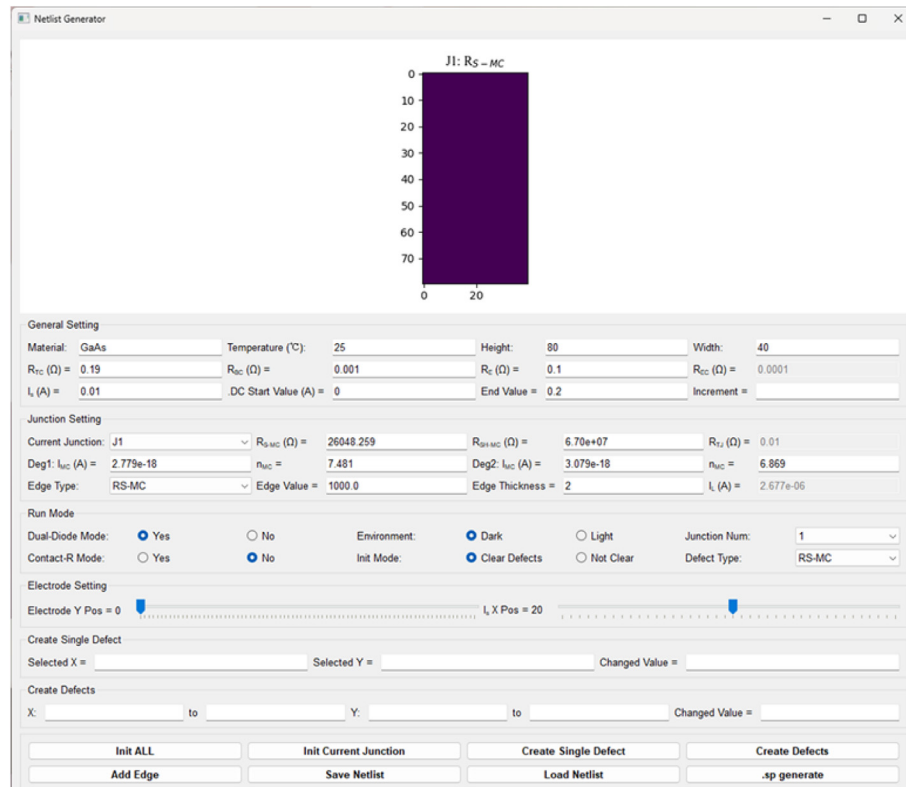


**Fig. 2.** User interface of the Netlist generator software.

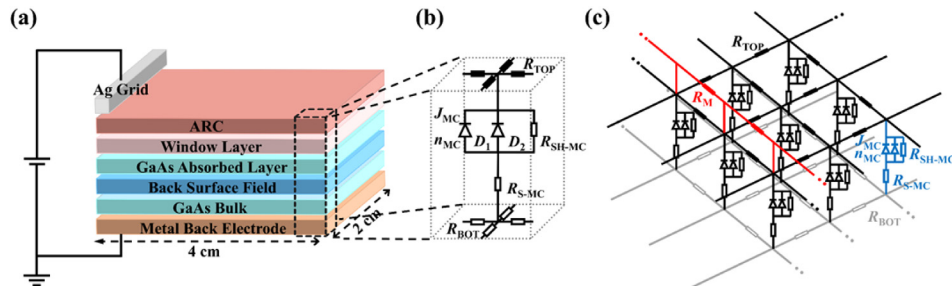


**Fig. 3.** (a) Schematic diagram of the GaAs solar cell sample utilized in this investigation. (b) Equivalent circuit model of a microcell within the solar cell, modeled using a two-diode approach in LED mode. (c) Part of the 3D distributed equivalent circuit model representing the cell for EL simulations.

**Table 2. Model Parameters of the Sample Solar Cell**

Electrical Parameters	40 × 20 Distributed Circuit Model	80 × 40 Distributed Circuit Model
$R_{S-MC} (\Omega \cdot \text{cm}^2)$	232	928
$R_{SH-MC} (\Omega \cdot \text{cm}^2)$	$8.16 \times 10^7$	$2.04 \times 10^7$
$J_{MC} (\text{A}/\text{cm}^2)$ for $D_1$	$7.68 \times 10^{-11}$	$1.92 \times 10^{-11}$
$n_{MC}$ for $D_1$	2.672	2.672
$J_{MC} (\text{A}/\text{cm}^2)$ for $D_2$	$1.608 \times 10^{-12}$	$4.02 \times 10^{-13}$
$n_{MC}$ for $D_2$	2.617	2.617
$R_{TOP} (\Omega/\square)$	0.17	0.17
$R_{BOT} (\Omega/\square)$	0.001	0.001
$R_M (\Omega/\square)$	0.1	0.1

dark mode. The parameters of the microcell conform to the following formula:  $J_{MC} = J/N$ ,  $n_{MC} = n$ ,  $R_{S-MC} = R_S \times N$ , and  $R_{SH-MC} = R_{SH}/N$  [28], where  $N$  represents the total number of microcells in the entire model. The sample solar cell is divided into  $80 \times 40$  microcells and  $40 \times 20$  microcells, and the parameters are shown in Table 2. It can be seen that the  $J_{MC}$ ,  $n_{MC}$ ,  $R_{S-MC}$ , and  $R_{SH-MC}$  between models with different accuracies have a proportional relationship consistent with the previous formula, and there are almost no differences between  $R_{TOP}$ ,  $R_{BOT}$ , and  $R_M$ .

Based on the reciprocity theorem introduced by Rau [40], the EL emission rate  $R_{EL}$ (photons/( $\text{s} \cdot \text{cm}^2$ )) under forward bias satisfies the following equation:

$$R_{EL}(E) = \text{EQE}(E) B(E) \exp\left(\frac{qV}{kT}\right), \quad (1)$$

where  $B(E)$  represents the spectral photon density of a black body,  $E$  represents the photon energy, and  $kT/q$  represents the thermal voltage. We used the SPICE software to extract the internal junction voltage of all microcells, and matched the edges and the shadow caused by the occlusion of the secondary electrode in the middle position of the sample represented by the actual EL images through numerical simulation. Figure 4(a) illustrates the absolute EL image obtained from the sample under experimental conditions at a temperature of  $25^\circ\text{C}$ , with a forward injection current density set at  $20 \text{ mA}/\text{cm}^2$ . This image provides a direct observation of the sample's EL characteristics under the given operational conditions. In comparison, Fig. 4(b) shows the corresponding simulated EL image, which is generated based on the  $80 \times 40$  distributed circuit model. The simulation functions as a theoretical counterpart to the experimentally captured data, providing insights into the expected EL behavior under similar conditions. In Fig. 4(c), the average EL

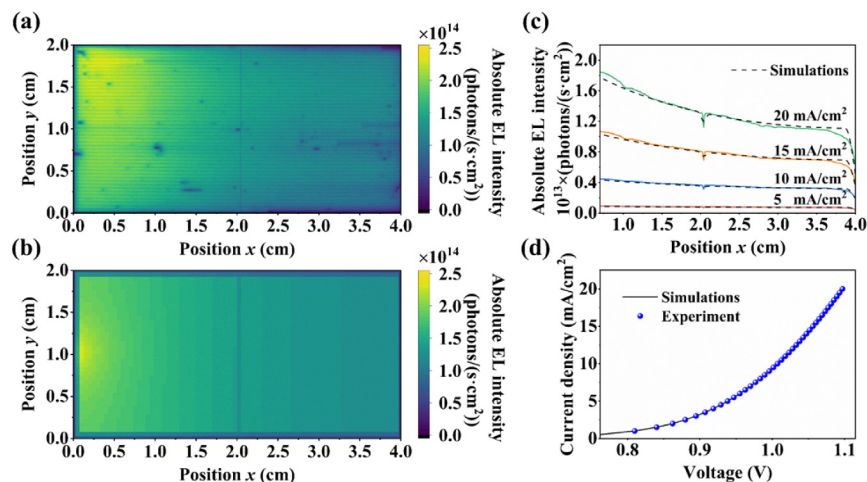


**Fig. 4.** (a) and (b) show the absolute EL images of the sample cell obtained through measurement and simulation ( $25^\circ\text{C}$ ,  $20 \text{ mA}/\text{cm}^2$ ). (c) The average EL intensities along the  $x$  direction for different injection current densities are presented, with measured data represented by solid lines and simulated data by dashed lines. (d)  $J - V$  characteristics of the sample cell in dark mode, with experimental data shown as scattered points and simulation results as a continuous line.

intensity values measured along the  $x$  direction of the GaAs solar cell are presented for different injection current densities. The simulation results model what happens to the system under the same conditions as the experimental results. Figure 4(d) finally depicts the  $J-V$  curve of the sample, which is obtained from the measurement (scatter points) and by the simulation (solid line) in dark mode. Figure 4 shows that the comparison between the experimental and simulated results across all four parts of Fig. 4 is strikingly broad and in good agreement, for the average EL intensity measured in the  $x$  direction across the sample and for the dark  $J-V$  curve. The strong correlation further validates the feasibility of using the proposed model as a good representation of the sample electrical and optical properties, and hence the proposed model will allow for a reliable dataset to be constructed prior to analysis and optimization.

### C. Defect Analysis

In the established equivalent circuit model, we artificially simulate localized defects by modifying the  $R_{S-MC}$  of microcells. Figures 5(a) and 5(b) show the normalized absolute EL image with four marked dark-spot defects of the sample cell and its simulation model. Figures 5(c) and 5(d) show the normalized absolute EL intensity and its loss rates, respectively, influenced by the injection current of one of the marked defects in the sample cell, with scattered dots representing experimental results and solid lines representing simulation results. The normalized absolute EL intensity loss rate is defined as

$$\eta = \left( \frac{I_{EL-D} - I_{EL-A}}{I_{EL-R}} \right) \times 100\%, \quad (2)$$

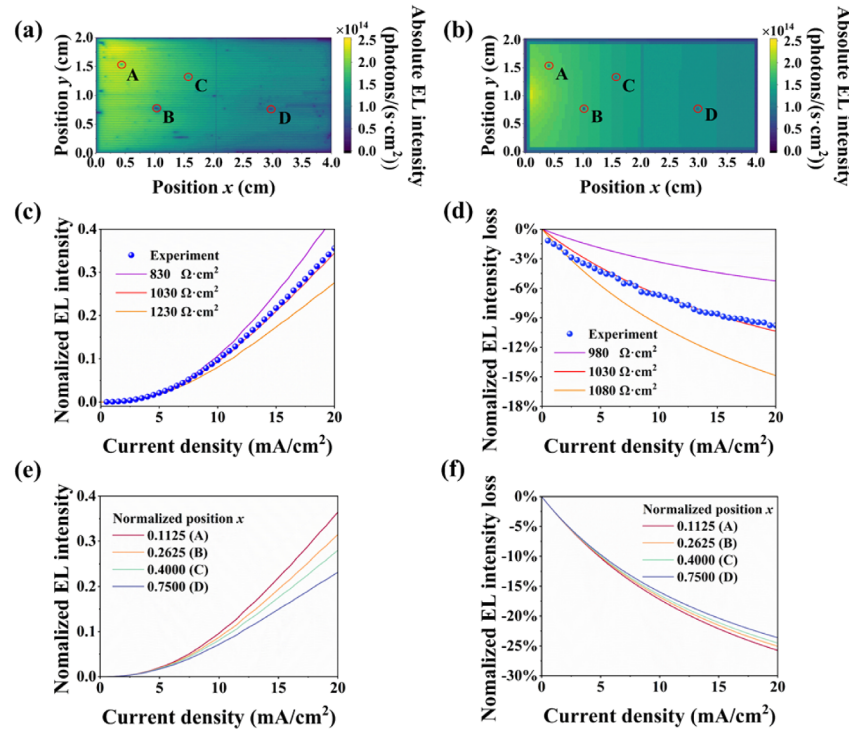


**Fig. 5.** Absolute EL images of a GaAs solar cell, obtained through measurement (a) and simulation (b), with four marked dark-spot defects ( $25^\circ\text{C}$ ,  $20\text{ mA/cm}^2$ ). Experimental and simulated results depict the normalized absolute EL intensity influenced by the injection current (c) and its loss rates (d) at the defect point C at different  $R_{S-MC}$  values. Normalized absolute EL intensity influenced by the injection current (e) and its loss rates (f) at the marked defects A, B, C, and D with the same  $R_{S-MC}$  ( $1200\ \Omega$ ) but different normalized position  $x$  ( $0.1125, 0.2625, 0.4000$ , and  $0.7500$ ).

where  $I_{EL-A}$  is the average absolute EL intensity within a  $5 \times 5$  square area around the defect,  $I_{EL-D}$  represents the defects' absolute EL intensity, and  $\eta$  denotes the normalized absolute EL intensity loss rate. It can be seen that artificially simulating black spot defects by increasing the  $R_{S-MC}$  in our simulation model has a good effect, and it also proves that  $R_{S-MC}$  has a strong correlation with the absolute EL intensity and its loss rates. Due to the influence of the sheet resistance in the top layer, the absolute EL intensity shows a noticeable decline along the  $x$  direction. This trend indicates that the current distribution across the sample is not uniform. In contrast, along the  $y$  direction, no significant reduction in the absolute EL intensity is observed. This suggests that the resistance effects in the top layer primarily affect the current flow and the corresponding EL emission in the  $x$  direction, with minimal impact in the perpendicular direction. Figures 5(e) and 5(f) show the normalized absolute EL intensity and its loss rates, respectively, influenced by the injection current of marked dark-spot defects with the same  $R_{S-MC}$  but different normalized  $x$  direction positions. It is evident that the location of a defect along the  $x$  direction plays a crucial role in determining the simulation outcomes. For defects with identical  $R_{S-MC}$  values, the farther the defect is from the electrode, the lower the normalized EL intensity becomes, as well as the associated loss rate, at a given current density. This indicates that the distance from the electrode significantly influences the EL performance and efficiency of the cell, even when defects share the same  $R_{S-MC}$  characteristics. In summary, we will use the absolute EL intensity influenced by injection current, its loss rates, and position  $x$  as input features for training the model.

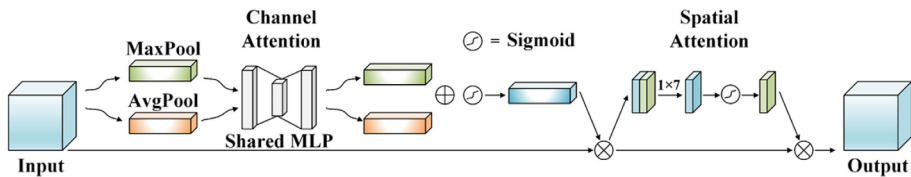


**Fig. 6.** Detailed structure of the CBAM module.

### 3. PROPOSED METHOD

#### A. Convolutional Block Attention Module

The correlation between the absolute EL intensity and its loss rate at different injection current densities results in a large amount of redundant information in the input data, which affects the accuracy of  $R_{S-MC}$  diagnosis. To overcome this challenge, we propose the use of the convolutional block attention module (CBAM), which selectively highlights important features and filters out irrelevant ones.

Figure 6 illustrates the structure of the CBAM, which consists of two primary components: the CAM and the SAM. The CAM is responsible for identifying and emphasizing the most relevant features, while the SAM is designed to focus on the spatial distribution and localization of these important features. The complete mechanism of the CBAM can be outlined as follows:

$$\begin{aligned} F' &= M_C(F) \otimes F \\ F'' &= M_S(F') \otimes F'. \end{aligned} \quad (3)$$

The CAM performs pooling operations on input features. These features are then forwarded to an MLP network separately, summed, and merged into the output feature vector through the sigmoid function. The mathematical formula for the CAM is shown in the following equation:

$$M_C(F) = \sigma(\text{MLP}(\text{AvgPool}(F)) + \text{MLP}(\text{MaxPool}(F))). \quad (4)$$

In this context,  $\sigma$  refers to the sigmoid function, which transforms input values into a continuous range from 0 to 1. The term  $F$  represents the input feature map, while the multilayer perceptron (MLP) includes two linear layers, activated by a ReLU function.

The CAM output is used as the input to the SAM, where pooling operations are performed along the channel dimension. Following this, a convolutional layer processes the pooled results using a filter of size  $1 \times 7$ . The mathematical formulation for the SAM is shown in the following equation:

$$M_S(F) = \sigma(f^{1 \times 7}([\text{AvgPool}(F); \text{MaxPool}(F)])), \quad (5)$$

where the operation  $f^{1 \times 7}$  refers to a convolution applied with a filter of size  $1 \times 7$ .

#### B. CBAM-MS-1DCNN

The core concept of a CNN involves constructing a multi-layer network that autonomously learns features from raw data and accumulates the learned features layer-by-layer. According to the convolutional kernel structure, CNN can be divided into one-dimensional CNN (1DCNN), two-dimensional CNNs

(2DCNN), and three-dimensional CNN (3DCNN). We established a 1DCNN model for the one-dimensional data extracted previously from absolute EL images. The model is built and tested using the Python machine-learning framework PyTorch.

This section focuses on the multi-scale concept in the Inception module and closely integrates it with the 1DCNN model and attention mechanism [41]. The Inception module's fundamental concept involves the integration of various convolutional and pooling operations to effectively capture input signals during model training. Following this, feature fusion is applied to the outputs from each operation path. This approach enables the network to extract more comprehensive features while maintaining spatial information of the input samples, ultimately enhancing detection accuracy. Moreover, it helps in optimizing the utilization of computational resources. As depicted in Fig. 7(a), the multi-scale convolution block (MSCB) processes the input data through multiple parallel pathways, utilizing  $1 \times 1$  and  $3 \times 3$  convolutions simultaneously. These paths provide different receptive fields for the network and finally fuse the extracted features. As shown in Fig. 7(b), we use two consecutive  $1 \times 3$  convolutional layers to equivalent a  $1 \times 5$  convolutional layer along one of the paths, reducing the number of parameters while maintaining the receptive field range.

Figure 7(c) illustrates the structure of the CBAM-MS-1DCNN model, while Table 3 outlines its detailed configuration. After the initial convolutional layer, a MaxPooling layer is applied. To minimize the number of parameters, an AvgPooling layer is placed after the final MSCB layer, replacing the need for a fully connected dense layer. A batch normalization (BN) layer follows each convolutional layer, with the ReLU activation function applied consistently. The performance was assessed based on the mean square error (MSE). During training, the Adam optimizer is utilized to minimize the MSE, with an initial learning rate set to 0.0001.

To effectively mitigate overfitting and improve the generalization ability of the model, L2 regularization was applied during training. L2 regularization introduces a penalty term to the loss function, proportional to the square of the model's weights, which discourages excessively large weight values and encourages the model to learn simpler feature representations. The strength of this regularization term is controlled by the regularization coefficient  $\lambda$ , which is set to  $1 \times 10^{-4}$  in this study. Additionally, batch normalization layers applied after each convolutional layer can stabilize the training process and improve generalization.

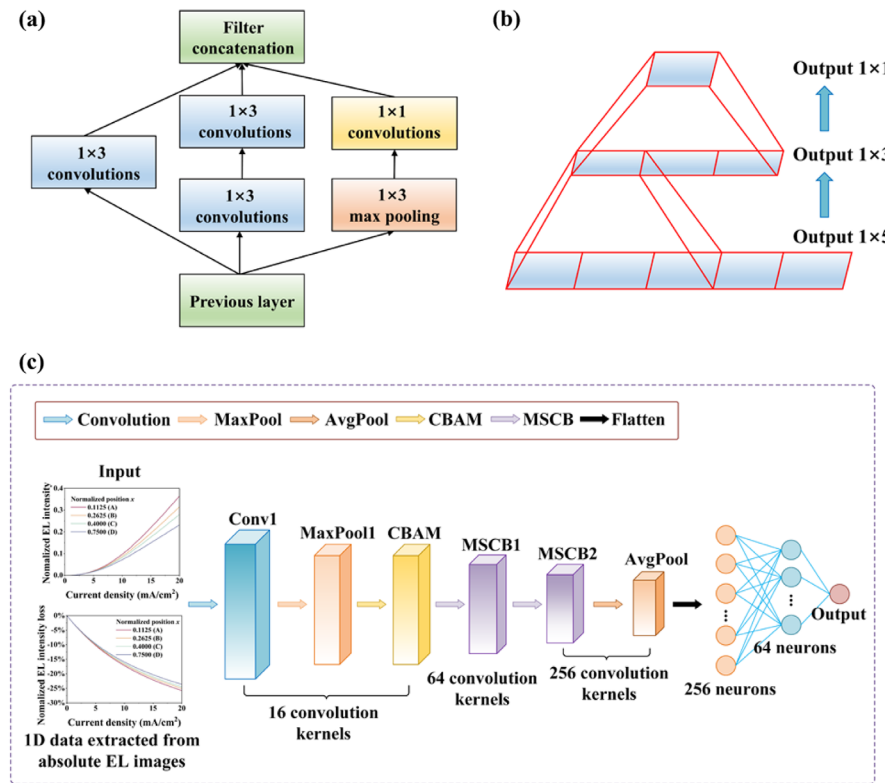


**Fig. 7.** (a) Structural diagram of the MSCB module. (b) Mini-network replacing the  $1 \times 5$  convolutions. (c) Network structure of the CBAM-MS-1DCNN model.

**Table 3. Structural Parameters of the CBAM-MS-1DCNN Model**

Layer	Kernel	Number of Kernels	Stride	Output
Input	—	—	—	$3 \times 40$
Conv1	$1 \times 3$	16	1	$16 \times 38$
MaxPool1	$1 \times 2$	16	2	$16 \times 19$
CBAM	—	16	—	$16 \times 19$
MSCB1	$1 \times 1, 1 \times 3$	64	2	$64 \times 9$
MSCB2	$1 \times 1, 1 \times 3$	256	2	$256 \times 4$
AvgPool	$1 \times 4$	256	1	$256 \times 1$
Flatten	—	—	—	256
Dense1	—	—	—	256
Dense2	—	—	—	64
Output	—	—	—	1

## 4. RESULTS AND DISCUSSION

### A. Dataset

We need to collect detailed experimental data of the sample solar cells under various injection current densities. Currently, there is no publicly available EL dataset that provides such comprehensive data. Therefore, it is necessary to use a self-generated dataset to train and test the model in this study. The dataset used in this study was generated using the “Netlist Generator” mentioned in Section 2.A, and the time cost for dataset creation is entirely acceptable.

To compromise between simulation accuracy and time consumption, we have divided the sample cell into  $40 \times 20$  microcells, yielding a total of 800 microcells, using the

parameters in Table 2 as the benchmark for the dataset. A higher-precision simulation model can be obtained by transforming the existing one using the formula in Section 2.B. We have established a dataset consisting of 250 simulation models, with a total of 200,000 defects. Our custom dataset is large in scale and encompasses a wide variety of defect conditions, which sufficiently demonstrates the generalizability of the proposed model. The  $R_{S-MC}$  of normal microcells fluctuates within a range of 5% around the  $R_{S-MC}$  of the benchmark model. We define a defect when the  $R_{S-MC}$  exceeds the normal value by 30%; therefore, the  $R_{S-MC}$  of a defect is set within the range of 280–1000  $\Omega$ . After processing in MATLAB, we extracted the absolute EL intensity influenced by the injection current, its loss rates, and position  $x$  as inputs. The  $R_{S-MC}$  was the output from each microcell of the simulation model used to train the CBAM-MS-1DCNN model. The variation range of the injected current density is  $0.5\text{--}20\text{ mA/cm}^2$ , with a step size of 0.5 mA. The input has been preprocessed, including normalization and deformation, and is composed of  $3 \times 40$  one-dimensional data. To evaluate the model’s accuracy, 80% of the dataset was allocated for training, while the remaining 20% was reserved for testing.

### B. Performance on the Training and Test Dataset

The CBAM-MS-1DCNN model was trained for 250 epochs using a normalized dataset, with a batch size of 512. During the training process, the loss values for both the training and validation samples were monitored and are shown in Fig. 8(a). As depicted in the figure, the model demonstrated steady convergence without exhibiting any signs of overfitting.

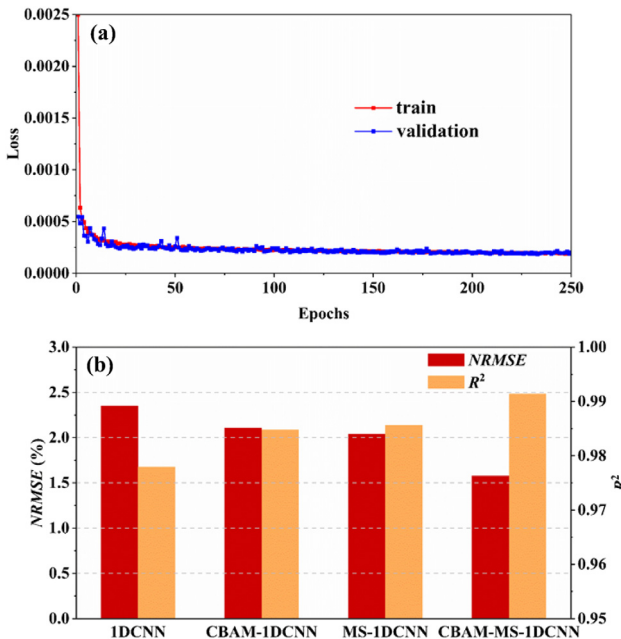


**Fig. 8.** (a) Training process of the CBAM-MS-1DCNN model. (b) Experimental comparison of NRMSE and  $R^2$  for different models.

Throughout the epochs, a clear downward trend in the loss value was observed, which gradually leveled off as the model reached stability. Specifically, the loss continued to decrease and showed signs of stabilization after approximately 80 epochs. By the 200th epoch, the training loss reached a value below 0.002, indicating that the model had successfully learned the underlying patterns without overfitting, and the training process had achieved the desired accuracy and efficiency. The model presents low oscillations after stabilization, indicating its robustness.

To better validate the applicability of the model, NRMSE and  $R^2$  were used as evaluation indicators for the prediction performance of  $R_{S-MC}$ . The formulas for  $R^2$  and NRMSE are as follows:

$$R^2 = 1 - \frac{\sum_{i=1}^n (y_i - \hat{y}_i)^2}{\sum_{i=1}^n (y_i - \bar{y})^2}, \quad (6)$$

$$\text{NRMSE} = \frac{\text{RMSE}}{y_{\max} - y_{\min}} = \sqrt{\frac{\sum_{i=1}^n (y_i - \hat{y}_i)^2}{n}}. \quad (7)$$

In this context,  $n$  denotes the number of samples included in the training set or the test set. The annotation of  $y_i$  is the actual value;  $\hat{y}_i$  is the predicted value;  $\bar{y}$  is the mean of the actual value;  $y_{\max}$  is the maximum actual value; and  $y_{\min}$  is the minimum actual value. We evaluated the performance of the CBAM-MS-1DCNN model against the 1DCNN, CBAM-1DCNN, and MS-1DCNN models using the test set. Figure 8(b) shows a comparison of NRMSE and  $R^2$  for the four different models, and Table 4 presents detailed experimental data. The CBAM-MS-1DCNN model has a low NRMSE, of 1.58%, and a high  $R^2$ , of 0.9914, on the test set, further verifying its good predictive ability for  $R_{S-MC}$ . After introducing MSCB layers and the CBAM layer in the 1DCNN model, the NRMSE decreased

**Table 4. Experimental Comparison of Different Models**

Model	NRMSE (%)	$R^2$
1DCNN	2.35	0.9779
CBAM-1DCNN	2.11	0.9848
MS-1DCNN	2.04	0.9856
CBAM-MS-1DCNN	1.58	0.9914

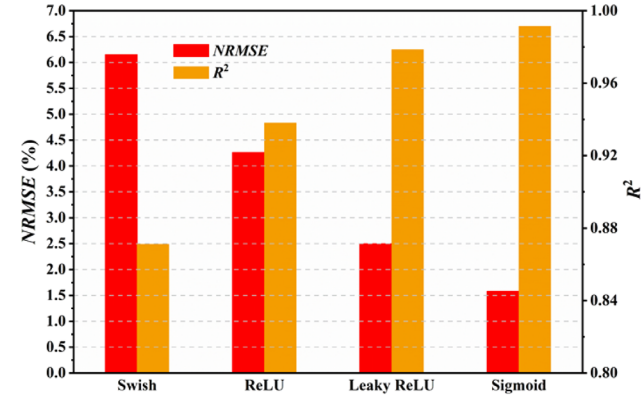


**Fig. 9.** Experimental comparison of NRMSE and  $R^2$  for CBAM with different activation functions.

**Table 5. Experimental Comparison of CBAM with Different Activation Functions**

Activation Function	NRMSE (%)	$R^2$
Swish	6.15	0.8711
ReLU	4.26	0.9380
Leaky ReLU	2.50	0.9786
Sigmoid	1.58	0.9914

and  $R^2$  increased, validating the rationality of the proposed improved model.

The activation function used in CBAM is sigmoid, which has been shown to be prone to causing vanishing gradient issues. To ensure the rigor of the experiments, we replaced the activation function in CBAM of the CBAM-MS-1DCNN model with Swish, ReLU, and Leaky ReLU, and performed a comparative analysis of the experimental results, as shown in Fig. 9. The detailed data are presented in Table 5. The results indicate that when using sigmoid as the activation function, the NRMSE is significantly lower, and the  $R^2$  is significantly higher compared to the other functions, highlighting the necessity of using sigmoid as the activation function in CBAM.

### C. Evaluation of the $R_{S-MC}$ Diagnosis

To verify the performance of the model for real GaAs solar cells, we extracted input data from the collected experimental images and predicted it using the proposed model. The detailed results are shown in Fig. 10. We first applied  $5 \times 5$  Gaussian filtering to an experimental absolute EL image ( $634 \times 324$  pixels), as shown in Fig. 10(a), and then slightly adjusted the size of the experimental image ( $640 \times 320$  pixels) and divided it into an average of  $80 \times 40$  pixel regions. The resized dimensions of 640 (height) and 320 (width) are integer multiples of the

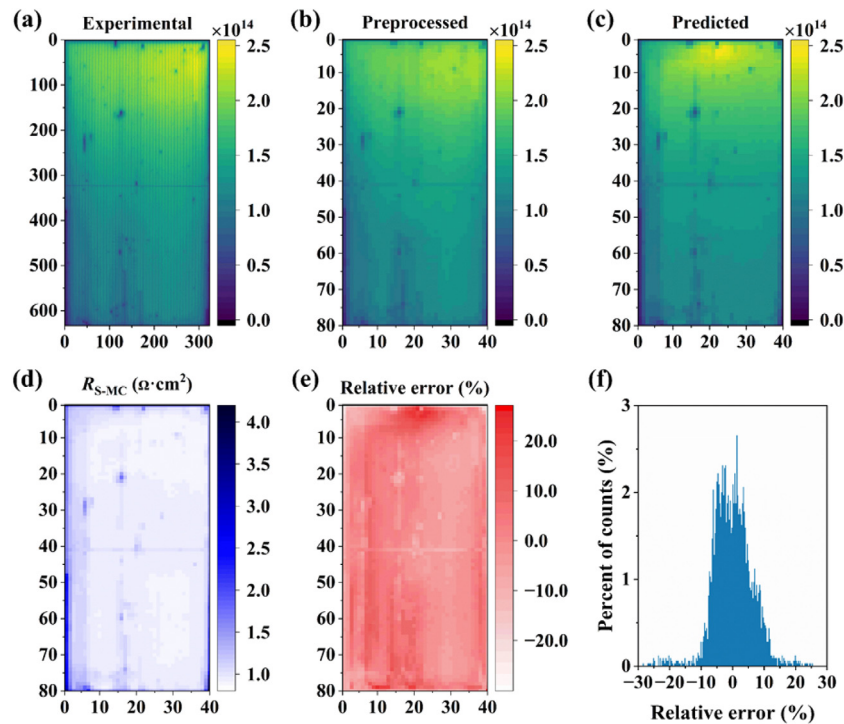


**Fig. 10.** (a) Absolute EL image ( $634 \times 324$  pixels) of the GaAs solar cell obtained through measurement ( $25^\circ\text{C}$ ,  $20 \text{ mA/cm}^2$ ). (b) Absolute EL image preprocessed by Gaussian filtering, slight resizing, and segmentation ( $80 \times 40$  pixels). (c) Absolute EL image obtained by simulating the  $R_{S-MC}$  map predicted by the CBAM-MS-1DCNN model. (d)  $R_{S-MC}$  map predicted by the CBAM-MS-1DCNN model. (e) Relative error map of the preprocessed image in (b) and the predicted one in (c). (f) Distribution of the relative error map in (e).

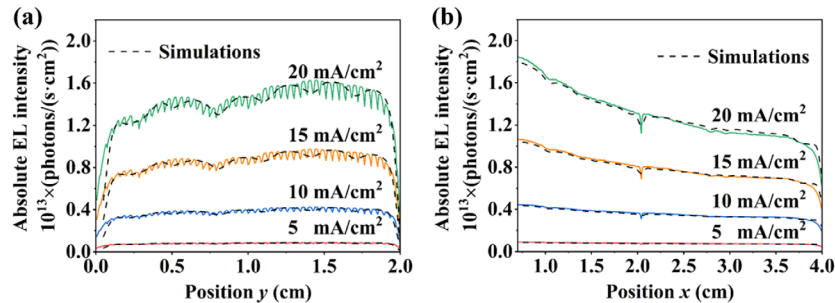


**Fig. 11.** Average EL intensities across the GaAs cell in the  $y$  direction (a) and  $x$  direction (b) for different injection current densities, with measured values represented by solid curves and predicted values by dashed curves.

circuit model's height (80) and width (40), ensuring convenient pixel division in subsequent processing. The final  $R_{S-MC}$  distribution is obtained based on an  $80 \times 40$  distributed circuit model, meaning that each microcell in the model corresponds to an  $8 \times 8$  pixel region of the preprocessed EL image. In the next step, we computed the average of the absolute EL intensity within each individual pixel region. This value was then considered as the representative absolute EL intensity for that specific region. The preprocessed absolute EL image is shown in Fig. 10(b). We calculated the  $R_{S-MC}$  distribution of the  $40 \times 20$  distributed circuit model using the CBAM-MS-1DCNN model and converted it into an  $80 \times 40$  one, as shown in Fig. 10(d). The  $80 \times 40$  distributed equivalent circuit model is established for the GaAs sample solar cell based on the predicted  $R_{S-MC}$  map and obtained the predicted absolute EL image, as shown in Fig. 10(c).

Comparing Figs. 10(b) and 10(c), it is evident that the predicted absolute EL image presents the approximate distribution of dark-spot defects in the experimental image and has good prediction performance for both independent dark-spot defects and continuous patches of dark-spot defects. Figure 10(e) presents a map showing the relative errors calculated between the images in Figs. 10(b) and 10(c). Additionally, Fig. 10(f) illustrates how the relative error values, displayed in Fig. 10(e), are distributed across the image. The predicted absolute EL image matches well with the experimental one, and the relative error of the absolute EL intensity in most pixel regions is within  $\pm 10\%$ , and the relative error of a few regions is around 20%. This proves the stability and practicality of the proposed model. The larger error in Fig. 10(f) can be attributed to the difference between the simulation model and the real solar cell, which affects the accuracy of the calculated defect loss rate. This issue is

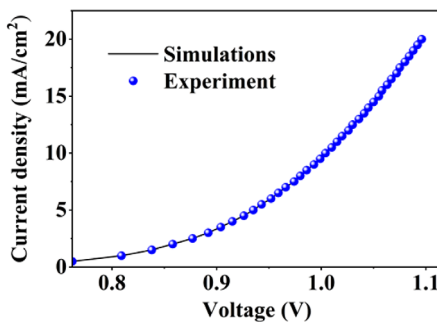


**Fig. 12.** Measured (scattered dots) and predicted (solid line)  $J-V$  curves of the GaAs cell in dark mode.

inevitable and beyond the scope of this article's discussion due to the experimental conditions.

Figures 11(a) and 11(b) present both the experimental and predicted average EL intensities measured across the GaAs cell, with the data shown for various injection current densities in both the  $y$  direction and the  $x$  direction. Due to the current model's accuracy, the gate electrode on the solar cell surface cannot be reflected in the predicted equivalent circuit model. Despite this limitation, the results suggest that the predicted data-based curves effectively capture the non-uniformity of absolute EL intensity on the surface of actual solar cell samples. Figure 12 compares the experimental dark  $J-V$  curve with the predicted one. These results demonstrate strong agreement between the prediction model and the sample cell in terms of electrical performance, confirming the model's reliability. The proposed method has been proven to be practical and applicable from various aspects.

## 5. CONCLUSION

This work proposed an automated quantitative defect diagnosis technique for GaAs solar cells based on absolute EL imaging and distributed circuit modeling. The CBAM-MS-1DCNN model is proposed to diagnose localized series resistance parameters in commercial-grade GaAs solar cells. We established a simulation model of the sample GaAs solar cell and demonstrated that the absolute EL intensity, influenced by the injection current and its loss rates, is highly correlated with the localized series resistance of the defect; the influence of defect position on the diagnosis results was also considered by the model. A medium-sized dataset containing 250 simulation models of 200,000 sets of data is constructed to train the CBAM-MS-1DCNN model, which provides a novel solution to the scarcity of EL datasets. The CBAM-MS-1DCNN model achieves good performance on the test set, with a minimum NRMSE of 1.35% and an  $R^2$  of 0.9914. Finally, the proposed model is shown to achieve strong predictive performance for real defects. Using the predicted parameters, a distributed equivalent circuit model is established to accurately simulate the electrical performance and absolute EL intensity distribution of real solar cells. This means that our approach is both practical and universally applicable. It is shown that the proposed method can be used by researchers to quickly set up a high precision distributed equivalent circuit model of GaAs solar cells and find the electrical characteristics of the whole solar cell and each defect. While this work focuses

on commercial-grade GaAs solar cells, future studies can explore the adaptability of the proposed CBAM-MS-1DCNN model to other photovoltaic technologies, such as perovskite, silicon, and multi-junction solar cells. Investigating the model's generalizability across different material systems could broaden its applicability. Additionally, an adaptive learning mechanism can be integrated into the CBAM-MS-1DCNN model to enhance its real-time defect diagnosis capability. By continuously updating the model with new experimental EL data and real-world defect patterns, the system can dynamically adjust its parameters to improve predictive accuracy over time.

**Funding.** National Natural Science Foundation of China (62274065, 62404103); National Key Research and Development Program of China (2024YFB4207102); Science and Technology Commission of Shanghai Municipality (24TS1400700); Natural Science Foundation of Chongqing Municipality (CSTB2023NSCQMSX1034).

**Disclosures.** The authors declare no conflicts of interest.

**Data availability.** Data underlying the results presented in this paper are not publicly available at this time but may be obtained from the authors upon reasonable request.

## REFERENCES

- M. A. Green, E. D. Dunlop, M. Yoshita, et al., "Solar cell efficiency tables (Version 64)," *Prog. Photovoltaics* **32**, 425–441 (2024).
- M. Al-Soeidat, T. Cheng, D. D. C. Lu, et al., "Experimental study of static and dynamic behaviours of cracked PV panels," *IET Renew. Power Gener.* **13**, 3002–3008 (2019).
- A. Bouich, J. Mari-Guaita, F. Baig, et al., "Investigation of the surface coating, humidity degradation, and recovery of perovskite film phase for solar-cell applications," *Nanomaterials* **12**, 3027 (2022).
- Z. Li, K. H. Chiu, R. S. Ashraf, et al., "Toward improved lifetimes of organic solar cells under thermal stress: substrate-dependent morphological stability of PCDTB:PCBM films and devices," *Sci. Rep.* **5**, 15149 (2015).
- U. Hijjawi, S. Lakshminarayana, T. Xu, et al., "A review of automated solar photovoltaic defect detection systems: approaches, challenges, and future orientations," *Sol. Energy* **266**, 112186 (2023).
- M. Barukcic, Z. Hederic, and Z. Spoljaric, "The estimation of I-V curves of PV panel using manufacturers' I-V curves and evolutionary strategy," *Energy Convers. Manage.* **88**, 447–458 (2014).
- Y. Tsuno, Y. Hishikawa, and K. Kurokawa, "Modeling of the I-V curves of the PV modules using linear interpolation/extrapolation," *Sol. Energy Mater. Sol. Cells* **93**, 1070–1073 (2009).
- M. Mazrouei, M. Pordel, A. Davoodnia, et al., "Synthesis and characterization of new purple and green heterocyclic dyes for dye-sensitized solar cells," *J. Mol. Struct.* **1315**, 138814 (2024).
- A. M. C. Silveira, M. R. M. Neves, R. Garcia, et al., "Characterization of solar cell busbar grid for different technologies by time domain reflectometry simulation: transmission line approach," in *IEEE 50th Photovoltaic Specialists Conference (PVSC)* (2023).
- M. M. Shehata and M. M. Makhlof, "Carrier transport mechanisms and photovoltaic performance of Ag/MoO<sub>x</sub>/Ag/MoO<sub>x</sub>/n-Si/C60/AI heterojunction solar cell," *J. Mater. Sci.* **35**, 597 (2024).
- M. A. Alenizi, M. Aouassa, M. Bouabdellaoui, et al., "Electrical and dielectric characterization of Ge quantum dots embedded in MIS structure (AuPd/SiO<sub>2</sub>:Ge QDs/n-Si) grown by MBE," *Physica B* **685**, 415962 (2024).
- B. Nath, B. Uppara, S. Singh, et al., "Exploring the potential of green synthesized ZnO-SnO<sub>2</sub> composite as an effective electron transport layer for perovskite solar cells: a sustainable approach," *Chem. Eng. Sci.* **296**, 120249 (2024).
- A. S. Chaudhary and D. K. Chaturvedi, "Analyzing defects of solar panels under natural atmospheric conditions with thermal image processing," *Int. J. Image Graph. Signal Process.* **10**, 10–21 (2018).

14. B. Wiengmoon, K. Kirtikara, C. Jivacate, *et al.*, "Quantifying the uniformity of solar cells using thermal imaging diagnosis," *Appl. Therm. Eng.* **70**, 350–360 (2014).
15. V. I. Smirnov, V. Andreevich Sergeev, A. A. Gavrikov, *et al.*, "The study of current localization in solar cells during the thermal resistance measurements," in *Moscow Workshop on Electronic and Networking Technologies* (2020), Vol. **5**, p. 5.
16. S. Deitsch, V. Christlein, S. Berger, *et al.*, "Automatic classification of defective photovoltaic module cells in electroluminescence images," *Sol. Energy* **185**, 455–468 (2019).
17. B. Su, H. Chen, and Z. Zhou, "BAF-detector: an efficient CNN-based detector for photovoltaic cell defect detection," *IEEE Trans. Ind. Electron.* **69**, 3161–3171 (2022).
18. B. Wu, K. Fu, N. Yantara, *et al.*, "Charge accumulation and hysteresis in perovskite-based solar cells: an electro-optical analysis," *Adv. Energy Mater.* **5**, 1500829 (2015).
19. U. Rau, B. Blank, T. C. M. Mueller, *et al.*, "Efficiency potential of photovoltaic materials and devices unveiled by detailed-balance analysis," *Phys. Rev. Appl.* **7**, 044016 (2017).
20. G.-J. A. H. Wetzelaer, M. Scheepers, A. Miquel Sempere, *et al.*, "Trap-assisted non-radiative recombination in organic-inorganic perovskite solar cells," *Adv. Mater.* **27**, 1837–1841 (2015).
21. I. Garcia, P. Espinet-Gonzalez, I. Rey-Stolle, *et al.*, "Analysis of chromatic aberration effects in triple-junction solar cells using advanced distributed models," *IEEE J. Photovoltaics* **1**, 219–224 (2011).
22. P. Espinet, I. Garcia, I. Rey-Stolle, *et al.*, "Extended description of tunnel junctions for distributed modeling of concentrator multi-junction solar cells," *Sol. Energy Mater. Sol. Cells* **95**, 2693–2697 (2011).
23. O. Breitenstein and S. Rissland, "A two-diode model regarding the distributed series resistance," *Sol. Energy Mater. Sol. Cells* **110**, 77–86 (2013).
24. S. Roy and R. Gupta, "Quantitative estimation of shunt resistance in crystalline silicon photovoltaic modules by electroluminescence imaging," *IEEE J. Photovoltaics* **9**, 1741–1747 (2019).
25. M. Kikelj, B. Lipovsek, M. Bokal, *et al.*, "Spatially resolved electrical modelling of cracks and other inhomogeneities in crystalline silicon solar cells," *Prog. Photovoltaics* **29**, 124–133 (2021).
26. S. Chen, L. Zhu, M. Yoshita, *et al.*, "Thorough subcells diagnosis in a multi-junction solar cell via absolute electroluminescence-efficiency measurements," *Sci. Rep.* **5**, 7836 (2015).
27. X. B. Hu, T. F. Chen, J. Y. Hong, *et al.*, "Diagnosis of GaAs solar-cell resistance via absolute electroluminescence imaging and distributed circuit modeling," *Energy* **174**, 85–90 (2019).
28. J. Hong, Y. Wang, Y. Chen, *et al.*, "Absolute electroluminescence imaging with distributed circuit modeling: excellent for solar-cell defect diagnosis," *Prog. Photovoltaics* **28**, 295–306 (2020).
29. Y. Wang, L. Li, Y. Jia, *et al.*, "Defect-induced current coupling in multi-junction solar cells revealed by absolute electroluminescence imaging," *Prog. Photovoltaics* **30**, 1410–1422 (2022).
30. Y. Jia, Y. Wang, X. Hu, *et al.*, "Electroluminescence imaging of laser induced defect formation in Cu(In, Ga)Se<sub>2</sub> solar cell," *Sol. Energy Mater. Sol. Cells* **230**, 111160 (2021).
31. Y. Jia, Y. Wang, X. Hu, *et al.*, "Diagnosing breakdown mechanisms in monocrystalline silicon solar cells via electroluminescence imaging," *Sol. Energy* **225**, 463–470 (2021).
32. Q. Huang, Y. Wang, X. Hu, *et al.*, "Effects of localized tensile stress on GaAs solar cells revealed by absolute electroluminescence imaging and distributed circuit modeling," *Sol. Energy* **274**, 112541 (2024).
33. Z. Luo, S. Y. Cheng, and Q. Y. Zheng, "GAN-based augmentation for improving CNN performance of classification of defective photovoltaic module cells in electroluminescence images," in *4th International Conference on New Energy and Future Energy System (NEFES)*, IOP Conference Series-Earth and Environmental Science (2019).
34. A. Ahmad, Y. Jin, C. Zhu, *et al.*, "Photovoltaic cell defect classification using convolutional neural network and support vector machine," *IET Renew. Power Gener.* **14**, 2693–2702 (2020).
35. X. Chen, T. Karin, and A. Jain, "Automated defect identification in electroluminescence images of solar modules," *Sol. Energy* **242**, 20–29 (2022).
36. N. Kellil, A. Aissat, and A. Mellit, "Fault diagnosis of photovoltaic modules using deep neural networks and infrared images under Algerian climatic conditions," *Energy* **263**, 125902 (2023).
37. H. Acikgoz, D. Korkmaz, and U. Budak, "Photovoltaic cell defect classification based on integration of residual-inception network and spatial pyramid pooling in electroluminescence images," *Expert Syst. Appl.* **229**, 120546 (2023).
38. Q. Liu, M. Liu, C. Wang, *et al.*, "An efficient CNN-based detector for photovoltaic module cells defect detection in electroluminescence images," *Sol. Energy* **267**, 112245 (2024).
39. M. Y. Demirci, N. Besli, and A. Gumuscu, "An improved hybrid solar cell defect detection approach using Generative Adversarial Networks and weighted classification," *Expert Syst. Appl.* **252**, 124230 (2024).
40. U. Rau, "Reciprocity relation between photovoltaic quantum efficiency and electroluminescent emission of solar cells," *Phys. Rev. B* **76**, 435 (2007).
41. C. Szegedy, V. Vanhoucke, S. Ioffe, *et al.*, "Rethinking the inception architecture for computer vision," in *IEEE Conference on Computer Vision and Pattern Recognition (CVPR)* (2016), pp. 2818–2826.